RESEARCH ARTICLE

X. Huang, Y. Yin, G. Saha, I. Francis,
S. C. Saha* 2400004

A Comprehensive Numerical Study on the Transport and Deposition of Nasal Sprayed Pharmaceutical Aerosols in a Nasal-To-Lung Respiratory Tract Model
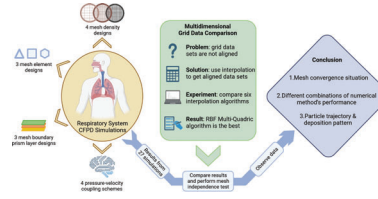
A state-of-the-art study evaluates various numerical schemes for fluid-particle simulations in a computed tomography-based respiratory tract model, revealing optimal mesh criteria, effective aerosol transport dynamics, and targeted particle deposition for nasal sprayed medications. Discover how these findings can revolutionize aerosol drug delivery.

A Comprehensive Numerical Study on the Transport and Deposition of Nasal Sprayed Pharmaceutical Aerosols in a Nasal-To-Lung Respiratory Tract Model

Xinlei Huang, Yaohui Yin, Goutam Saha, Isabella Francis, and Suvash C. Saha*

Utilizing a computed tomography (CT)-based realistic nasal-to-lung respiratory tract model allows for a comprehensive investigation of the transport and deposition of nasal sprayed aerosols. This study has three main objectives: first, to determine the optimal mesh that achieves the quickest convergence for computational fluid-particle dynamics (CFPD) simulations of a nasal-to-lung nasal respiratory tract by assessing the performance of different element types, sizes, and prism boundary layers; second, to design and validate a numerical method to compare grid data with different mesh structures and densities for simulation result validation; and finally, to observe and analyze fluid-particle dynamics in the respiratory tract to aid in the development of nasal sprayed medications. This study involves reverse-engineering a realistic and anatomically accurate respiratory tract model from CT scans. Results reveal that the optimal numerical approach for minimum calculation time is the polyhedral hybrid mesh with four boundary prism layers and the SIMPLE pressure-velocity coupling scheme. Furthermore, observations of particle dynamics reveal that the vocal cords' location contains a concentration site of deposited small aerosols due to the turbulent airflow in the region. The optimal diameters of nasal sprayed aerosols to target each region are concluded in the end.

1. Introduction

Assessments of respiratory morphology for abnormalities and disorders, analysis of inhalation toxicity, and prediction of the local dosage received from medication aerosols are feasible through the use of three dimentional 3D computational models. In the past several decades, there has been a discernible rise in the use of computational fluid dynamics (CFD)[1] for biomedical investigations[2] of the human airway. For example, Inthavong et al.[3] examined many numerical approaches that were employed in the respiratory system CFD analyses from 1993 to 2017. A selection of computational fluid-particle dynamics (CFPD) studies from 2018 to 2024 is presented in **Table 1** to supplement their literature review.

Due to the intricate geometry of the respiratory tract and the presence of turbulent airflow, researchers have turned to computational modeling for insights into the transport and deposition of nasal sprayed aerosols. Previous studies have explored the effects of anatomy and aerosol diameter on nasal sprays and nebulizers within nasal cavity geometries.[18,19] Additionally, researchers have investigated the relationship between nasal spray drug deposition patterns and pharmacokinetic profiles,[20] and the absorption and clearance of aerosols in the human nasal cavity.[21] Calmet et al.[22] conducted experiments to validate their numerical model of nasal spray particle deposition. Keeler et al.[23] conducted computational simulations in nasal cavities from four ethnic groups. Apart from nasal sprayed aerosols, major advancements have been made by Longest and his collaborators in terms of oral inhaled particles,[24–29] whole-lung simulations of aerosols,[16] and boundary layer mesh investigation for particle dynamics.[30] Xi and his collaborators have also made major contributions in modelling oral inhaled aerosols[31,32] and nasal spray in the nasal cavity.[33–35]

However, the increasing utilization of CFPD applications is not accompanied by a rigorous numerical validation process. As illustrated in Table 1, most recent CFPD studies do not provide details regarding the specific numerical validation methods employed. Furthermore, many of these studies rely on 1D or averaged values as convergence indicators, without addressing the global or local convergence status. Adopting rigorous grid convergence criteria, such as the GCI, remains an uncommon practice in this context, primarily due to the

X. Huang, G. Saha, I. Francis, S. C. Saha
Faculty of Engineering and Information Technology
University of Technology Sydney
Sydney, New South Wales 2007, Australia
E-mail: suvash.saha@uts.edu.au
Y. Yin
Vehicle & Transportation Engineering Institute
Henan University of Science and Technology
Luoyang, Henan 471003, China

ADVANCED
SCIENCE NEWS

www.advancedsciencenews.com

Particle
& Particle Systems Characterization

www.particle-journal.com

Table 1. A selection of 2018 to 2024 literature on CFPD respiratory tract simulation.

Refs.	Geometry	Turbulence Models	Max Cell Number	Mesh Type[a]	Convergence Evaluation
[4]	Discontinuous G0-15[b]	Realizable k-ϵ	0.68	T	Averaged value & 1D
[5]	Symmetrical G0-11	k-ω SST	1	TP	Not specified
[6]	Symmetrical G0-14	Realizable k-ϵ	1.9	PP	Averaged value & 1D
[7]	Oral cavity-G3	Realizable k-ϵ	4.57	TP	Averaged value & 1D
[8]	Nasal cavity-G3	k-ω LRN	4.9	TP	GCI[c]
[9]	Oral cavity-G6	k-ω SST	6	TP	Not specified
[10]	Idealized G0-17	k-ω SST	6.7	PP	Not specified
[11]	Nasal cavity-G13	k-ω SST	7.6	PP	1D
[12]	Oral cavity-G10	k-ω SST and DES	9.7	TP & PP	Not specified
[13]	Upper airway	LES	10	TP	Not specified
[14]	Upper airway	k-ω LRN	11.5	TP & PP	Averaged value
[15]	Oral cavity-G5	k-ω LRN	12.1	TP	1D
[16]	Symmetrical G0-acinus region	Lagrangian-Eulerian framework	16.5	T	Not specified
[17]	Oral cavity-G12	k-ω SST	20	TP	1D

[a] T is tetrahedral mesh, TP is tetrahedral mesh plus near-wall prism layers, PP is polyhedral mesh plus near-wall prism layers; [b] G is airway generation, as illustrated in Figure 1; [c] Grid Convergence Index.

challenges associated with numerically validating results within the complex geometry of human airways. Several studies have focused on evaluating the accuracy of CFD solutions and addressing methodological uncertainties in the validation process. For bronchial tubes, Soni and Thompson[36] found primary flow independence with low-density meshes but no grid convergence for secondary flow. Longest and Vinchurkar[37,38] used GCI for convergence assessment. Meanwhile, Soni et al.[39] conducted a mesh refinement study on an idealized nine-generation airway model. Zubair et al.[40] observed discrepancies between hybrid and unstructured grids. Frank-Ito et al.[41] improved hybrid mesh investigation, requiring ≈4 million cells for grid independence for the nasal airways model, a result that is twice as many as that of Zubair et al.[40] The pressure-velocity coupling scheme study of Kumar et al.[42] found the pressure-implicit with splitting of operators scheme ideal for steady-state flow modeling.

Most research, including all the mesh evaluation studies mentioned above, was conducted on idealized and incomplete respiratory airway geometries. Furthermore, previous CFPD studies[7,9,27–29,43] employing simplified geometries may lack sufficient geometrical details to simulate the complex airflow-particle dynamics in the larynx region. The present study, however, conducts CFPD simulations in a state-of-the-art realistic respiratory tract geometry where the fate of nasal sprayed aerosols can be investigated with greater accuracy and detail. We created 18 meshes to determine the optimal mesh element type and boundary prism layer configuration, assessed based on their ability to deliver precise predictions while achieving the quickest convergence. We proposed a novel method to evaluate multidimensional grid convergence that compares unstructured meshes with varying element types and densities. This method was subjected to rigorous testing and evaluation to ensure its validity. Subsequently, the transport and deposition of nasal sprayed pharmaceutical aerosols with a 1 to 350µm[44] diameter range was ex-

amined. This work's distinctive attributes include polydisperse nasal sprayed aerosols, a nasal-to-lung realistic respiratory tract mimicking real-life conditions, an improved multidimensional grid convergence examination method, and an optimal mesh for CFPD applications.

1.1. Respiratory Tract

The human respiratory system comprises two main zones: The conducting zone (nose to bronchioles), responsible for transmitting airflow, and the respiratory zone (alveolar duct to alveoli), where gas exchange occurs. **Figure 1** illustrates the complete respiratory tract and the corresponding regions. The tracheobronchial tree depicted in Figure 1 and the remainder of the paper adhere to Weibel's model[45] for generation labeling.

2. Methodology Computational Model Creation

This investigation entailed the development of a realistic human respiratory tract computational model. Using Mimics Medical 21.0, we successfully segmented two distinct 3D surface models from two sets of CT images due to the unavailability of a single set of computed tomography (CT), scans providing clear views of both the bronchioles and nasal cavity. The first model encompassed the nasal cavity to the upper trachea, while the second model spanned from the trachea to the 13th-generation bronchioles. Details of the CT images used are presented in **Table 2**. The utilization of these CT images has been granted ethical permission by the Human Research Ethics Committees at the University of Technology Sydney.

Subsequently, the stereolithographic (STL) surface models were exported to Geomagic Wrap 2021, a commercial program
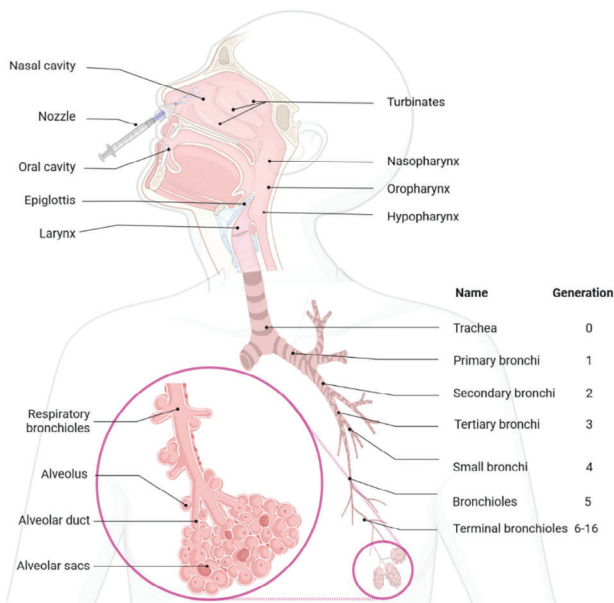
**ADVANCED
SCIENCE NEWS**

www.advancedsciencenews.com

Particle
& Particle Systems Characterization

www.particle-journal.com

Figure 1. An image showing: 1) Detailed labeling of the respiratory tract, starting from the nasal and oral cavities passing through the various lung generations, reaching the alveolar sacs at the distal lung. 2) Nasal spray into the nasal cavity.
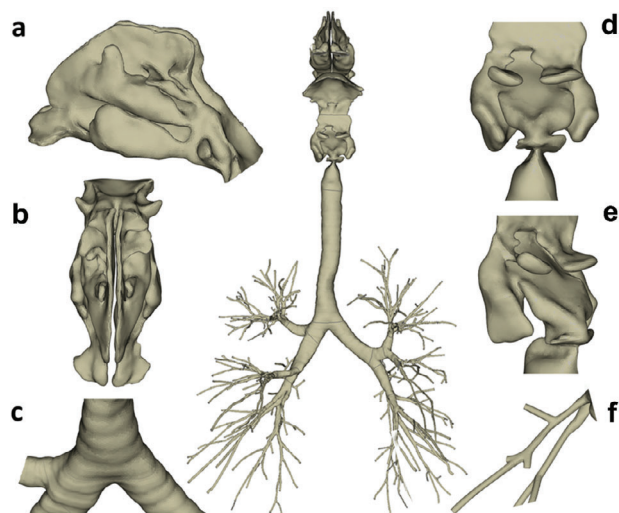

Figure 2. Computational model of respiratory tract used for mesh generation; a–f) enlarged local views of the model, where (a) and (b) present oblique and top view of the nasal region geometry, respectively; c) oblique view of the primary bronchi; d,e) front and oblique views of the larynx region, respectively; and f) oblique view of a section of terminal bronchioles.

enabling orderly patch division, facilitating sectioning and labeling in subsequent stages. Further post-processing was conducted using Siemens NX 12 before merging the surface models within meshing software. Our previous work[46–49] offers additional information regarding model post-processing. The final model of the respiratory tract is depicted in **Figure 2**.

For meshing and simulation convenience, the respiratory tract is divided into several regions, including the Nasal cavity (including Nasopharynx), Oral cavity (including Oropharynx), Larynx (including partial Laryngopharynx), Trachea, Primary Bronchi, Secondary Bronchi, Tertiary Bronchi, and different lobes (right superior, right middle, right inferior, left superior, and left inferior), as shown in **Figure 3**. **Figure 4** provides detailed sectioning of lung generations, starting from the trachea (generation 0) and ending with the terminal bronchioles in generation 14. The dimensions of our model, including inlets, outlets, and regions, are presented in **Table 3**, which specifies the number, surface area, and volume of these components. The inlets correspond to the two nostrils, the outlets represent the exits of the farthest lung generations, and the regions encompass the lung lobes and other main parts mentioned in Figure 3.

2.1. Mesh Configurations

2.1.1. Mesh Element Type

This study examines three meshconfiguration designs, namely tetrahedral hybrid, hexahedral hybrid, and polyhedral hybrid, as illustrated in **Figure 5**. The tetrahedral hybrid design features triangular prism (pentahedron) layers, with the remaining inner volume populated by triangular pyramid (tetrahedron) cells. In the polyhedral hybrid design, the boundary layer primarily consists of heptagonal and pentagonal prisms, with occasional trapezoidal or pentagonal prisms at some locations. The remainder of the volume is composed of irregular polyhedron cells. The hex-

Table 2. Parameters and data on the two CT scan image sets.

Parameters	Head CT	Thorax CT
Age	38	37
Image Resolution	512×512	512×512
Pixel Spacing [mm]	0.57	0.625
Slice Increment [mm]	0.5	0.5
Slice Thickness [mm]	1	1
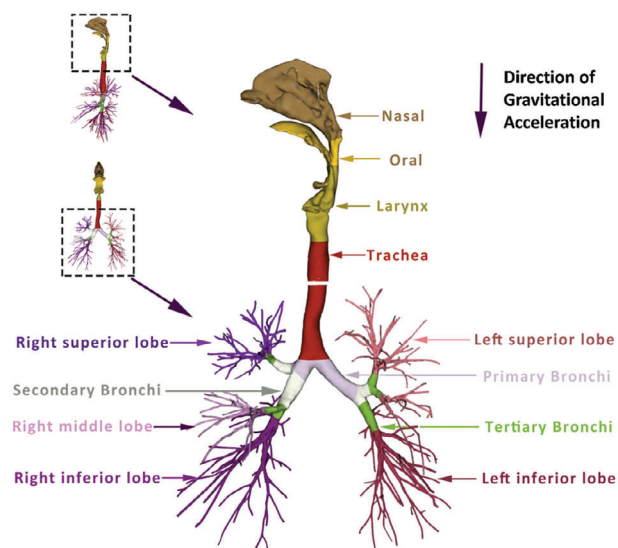
Figure 3. Respiratory tract regions and lung lobes.

**ADVANCED
SCIENCE NEWS**

www.advancedsciencenews.com

Particle
& Particle Systems Characterization

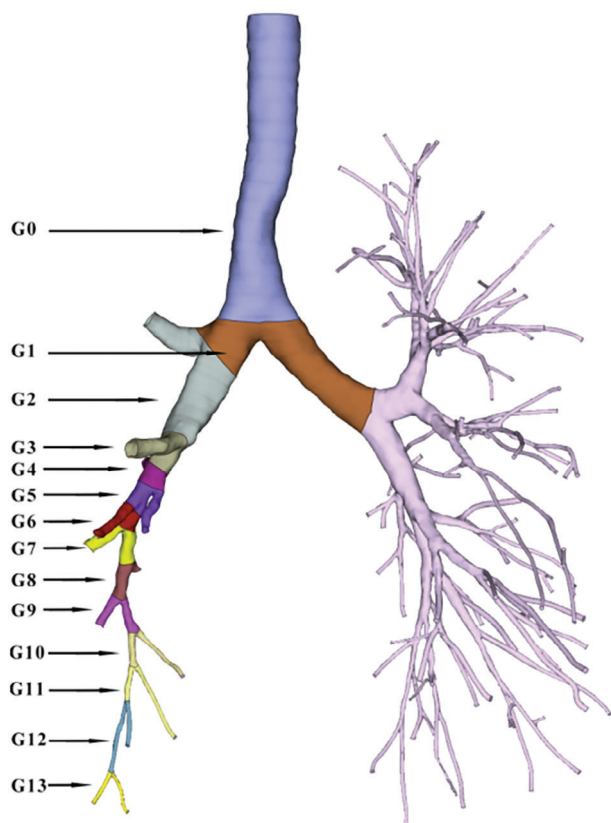www.particle-journal.com

Figure 4. Lung generation labeling in our realistic lung model, starting from generation 0 (trachea) to generation 13.

Table 3. Surface area, volume, number of inlets, outlets, and regions in the respiratory tract geometry.

Inlets	Surface Area [mm²]	Number
Nostril inlet (right)	93.11	1
Nostril inlet (left)	75.99	1

Outlets	Surface Area [mm²]	Number
Right superior lobe outlets	54.59	49
Right middle lobe outlets	26.53	23
Right inferior lobe outlets	53.08	47
Left superior lobe outlets	57.94	57
Left inferior lobe outlets	62.01	52
Total outlets	254.15	228

Region	Surface Area [mm²]	Volume [mm³]
Nasal	17 308.09	31 537.88
Oral	5038.05	9413.07
Larynx	4973.16	11 508.80
Trachea	5438.99	20 256.35
Primary Bronchi	1991.67	6094.52
Secondary Bronchi	1701.79	4071.09
Tertiary Bronchi	1982.72	4962.23
right superior lobe	4225.43	1765.20
right middle lobe	3163.99	1615.57
right inferior lobe	7047.43	3946.46
left superior lobe	6803.61	3066.26
left inferior lobe	6837.88	3474.33
Total	66 512.81	101 711.76

ahedral hybrid design incorporates triangular prism layers, with the inner volume being filled with hexahedron mesh cells.

2.1.2. Mesh Density

In this study, mesh density is controlled by adjusting the density of boundary nodes. Higher boundary node density results in more nodes on the surface and inside the volume, indirectly determining the total number of cells in the mesh. **Table 4** presents the total number of cells and nodes for each mesh design, where an increase in boundary node density from density-1 to density-4 leads to a successive 1.5-fold increase in the total number of cells in tetrahedral hybrid meshes (9, 13, 20, and 30 million). Initially, a low-density mesh is implemented to identify flow field turbulent intensity, which observes higher turbulent intensity at the larynx region (Figure S1, Supporting Information), consistent with previous studies.[42] Accordingly, the larynx region is meshed with a smaller surface boundary nodal distance. **Table 5** depicts the final boundary node density design indicating the average distance (in millimeters) between two nodes on the surface boundary, with four successive mesh refinements.

2.1.3. Boundary Layer

As near-wall mesh layers have an impact on particle deposition fraction in nasal cavity CFPD simulations,[41] three near-wall mesh layer configurations are examined (four, six, and eight prism cell layers) to determine the optimal number of layers required to accurately predict particle deposition in the whole respiratory tract model. A near-wall mesh refinement setup is adopted with the first cell height specified as 8% of the average of the surrounding nodal distances. In this way, the first cell height is calculated based on the local mesh density to adjust for geometrical changes from the nasal cavity to terminal bronchioles, as shown in **Figure 6**. Otherwise, applying the same cell height as the nostril opening would result in terminal bronchioles filled with prism layers.

Therefore, 18 distinct mesh configurations are considered comprising different mesh element types (tetrahedral, hexahedral, and polyhedral), mesh elements count (densities 1 to 4), and boundary layers number (4, 6, and 8). **Table 6** presents the abbreviated denominations of the various mesh designs.

2.2. Mesh Independence Test

2.2.1. Interpolation Schemes

Multiple regression analyses and interpolation techniques have been employed to tackle several challenges related to unstructured grid convergence. One challenge includes the inability to
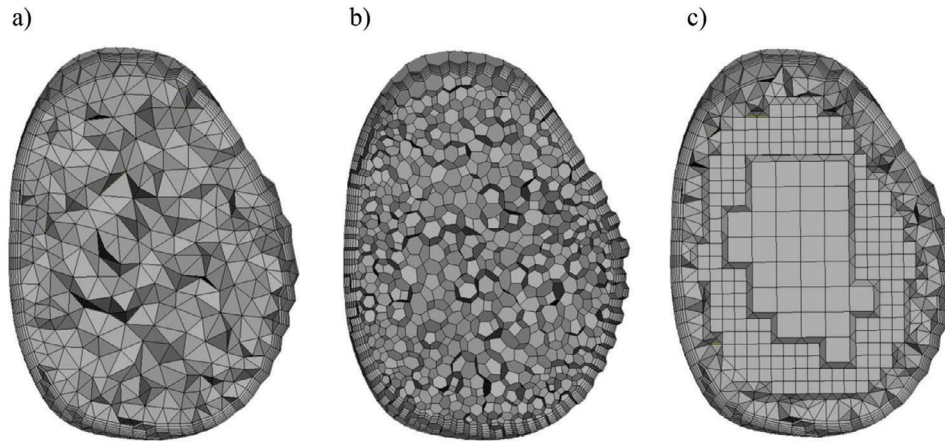
Figure 5. Cross-section of the meshed models at the same location in the trachea with three different mesh element types: a) tetrahedral hybrid; b) polyhedral hybrid; and c) hexahedral hybrid.

acquire a systematic and quantifiable grid refinement index,[50] and another is the difficulty in quantifying the differences between solution data from meshes with varying element compositions and densities. Using SciPy's nearest algorithm,[51] Inthavong et al.[3] interpolated unstructured grid data onto a uniform grid with higher density. However, this approach stretches the grid data to conform to the uniform grid shape, which may result in boundary concerns and inaccuracies. Longest and Vinchurkar[37,38] utilized a different technique to circumvent the boundary problem by selecting 1000 points inside the 2D plane and at consistent positions for interpolation. This study follows a comparable approach, creating a finer mesh at any desired line or plane. The coordinates of the nodes or cell centroids of the mesh, which serve as the locations of the interpolated points, are then exported from the meshing program. This study generated 12 sets of interpolated points on two different planes using a variety of interpolation intervals to determine the optimal number of interpolated points with a minimum effect on the interpolation result (Figures S2 and S3, Supporting Information).

As interpolation techniques may yield errors and boundary concerns, surface graphs are generated for visualization of the interpolation schemes' performance, comparing MATLAB's griddata nearest, griddata linear, griddata cubic, radial basis function (RBF) linear, RBF cubic, and RBF multi-quadric[52]

schemes' performance on various meshes (**Figure 7**; Figure S4, Supporting Information). Since an ordinary air velocity profile displays a smooth shape without steps (Figure 7a) or spikes (Figure S4f, Supporting Information), the RBF multi-quadric algorithm appears to provide the most reasonable and seamless prediction for the gaps between the original data (Figure 7b).

2.2.2. Governing Equations of the Selected Interpolation Method

Calculating the residual between two distinct grid data sets indicates the mesh's tendency to converge, helps in determining the correct density of the interpolated points, and evaluates the efficacy of different interpolation strategies. The formula for calculating the residual is the following:

$$\sigma = \frac{1}{N} \sum_{i=1}^{N} \frac{|q_i - p_i|}{(|q_i| + |p_i|)/2} \times 100\% \qquad (1)$$

The RBF function can be expressed as:

$$f(x) = c_0 + c_1 x + \sum_{i=1}^{n} \lambda_i \varphi(|x - x_i|) \qquad (2)$$

Table 4. Total number of cells and nodes in each mesh design.

	Tetrahedral Hybrid × 10⁶	Hexahedral Hybrid × 10⁶	Polyhedral Hybrid × 10⁶
Density − 1	9.17	8.94	4.86
Density − 2	13.13	13.20	6.20
Density − 3	20.25	22.18	8.56
Density − 4	29.52	30.02	11.71
Density − 4 2 less layers	24.23	24.82	8.82
Density − 4 2 more layers	34.18	34.23	14.62

Table 5. Surface boundary nodal distance (in millimeters) for each region with four successive mesh refinements.

Region	Density − 1	Density − 2	Density − 3	Density − 4
Nasal	0.85	0.8	0.75	0.725
Oral	0.85	0.8	0.75	0.725
Larynx	0.55	0.5	0.45	0.425
Trachea	0.85	0.8	0.75	0.725
Primary Bronchi	0.65	0.6	0.55	0.525
Secondary Bronchi	0.45	0.4	0.35	0.325
Tertiary Bronchi	0.3	0.25	0.2	0.165
Five Lobes	0.3	0.25	0.2	0.165

ADVANCED
SCIENCE NEWS
www.advancedsciencenews.com

Particle
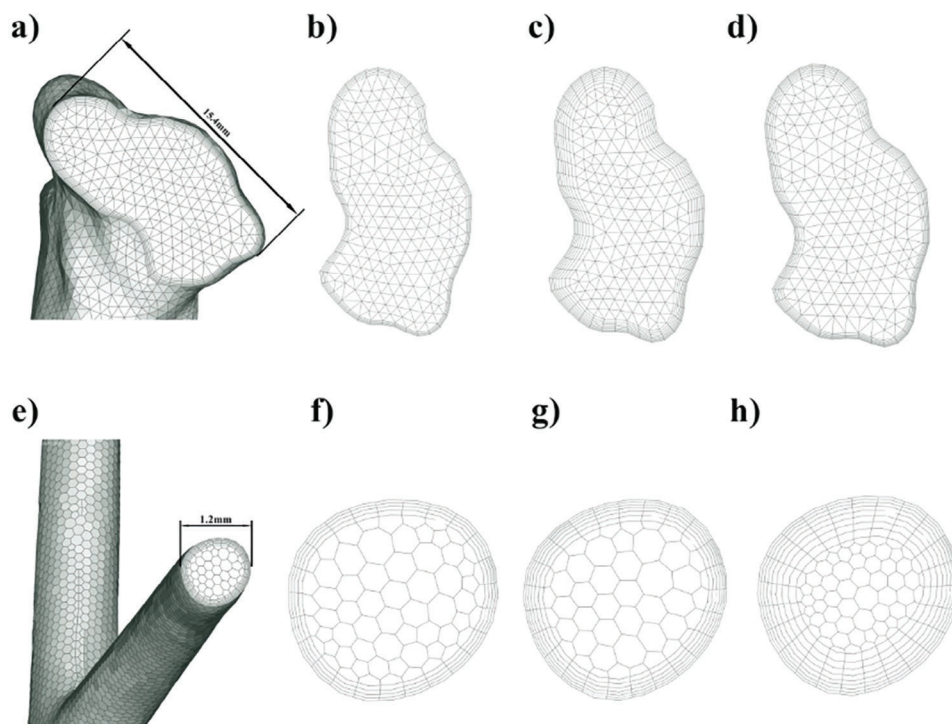& Particle Systems Characterization
www.particle-journal.com

Figure 6. Near-wall prism layers of the tetrahedral hybrid mesh at a nostril inlet and the polyhedral hybrid mesh at a bronchiole's outlet. a) Left nostril opening; b) 4 prism layers; c) 6 prism layers; and d) 8 prism layers. e) A bronchiole's outlet in the right superior lobe; f) 4 prism layers; g) 6 prism layers; and h) 8 prism layers.

where the multi-quadric method uses:

$$\varphi \left(|x - x_i| \right) = \sqrt{1 + \frac{r^2}{\sigma_m^2}} \tag{3}$$

2.3. Fluid and Particle Modeling

2.3.1. Governing Equations

The Navier–Stokes equations are used to solve for the movement of the continuum phase (airflow), and the Euler-Lagrange approach is employed for the dispersed phase (particles). The turbulence model used is $k - \omega$ SST, which incorporates the benefits of both the $k - \epsilon$ and $k - \omega$ models for aerodynamic flows[53] and predicts adverse pressure gradients without difficulty. The force

Table 6. Mesh configurations for 18 simulations.

Boundary Prism Layer Number	Boundary Node Density	Tetrahedral Hybrid	Hexahedral Hybrid	Polyhedral Hybrid
6	Density – 1	T1	H1	P1
6	Density – 2	T2	H2	P2
6	Density – 3	T3	H3	P3
6	Density – 4	T4	H4	P4
4	Density – 4	T5	H5	P5
8	Density – 4	T6	H6	P6

balance and tracking of particles account for the drag, gravity, Saffman's lift, and discrete random walk. The governing equations of the continuum and discrete phases are as follows:

Continuity equation:[54]

$$\frac{\partial \rho}{\partial t} + \nabla \cdot (\rho \boldsymbol{u}) = 0 \tag{4}$$

Momentum equation:[55]

$$\frac{\partial \rho \boldsymbol{u}}{\partial t} + \nabla \cdot (\rho \boldsymbol{u}\boldsymbol{u}) = -\nabla p + \nabla \cdot \left(\overline{\overline{\tau}} \right) + \rho \boldsymbol{g} \tag{5}$$

The turbulence kinetic energy (k) equation:[56]

$$\frac{\partial (\rho k)}{\partial t} + \frac{\partial (\rho k u_i)}{\partial x_i} = \frac{\partial}{\partial x_j} \left[\left(\mu + \frac{\mu_t}{\sigma_k} \right) \frac{\partial k}{\partial x_j} \right] + P_k - Y_k + G_b \tag{6}$$

The specific dissipation rate (ω) equation:[56]

$$\frac{\partial (\rho \omega)}{\partial t} + \frac{\partial (\rho \omega u_i)}{\partial x_i} = \frac{\partial}{\partial x_j} \left[\left(\mu + \frac{\mu_t}{\sigma_\omega} \right) \frac{\partial \omega}{\partial x_j} \right] + P_\omega - Y_\omega + G_{\omega b} \tag{7}$$

Particle trajectory equation:[57]

$$\frac{\partial \boldsymbol{x}}{\partial t} = \boldsymbol{u}_p \tag{8}$$

ADVANCED
SCIENCE NEWS

www.advancedsciencenews.com

Particle
& Particle Systems Characterization
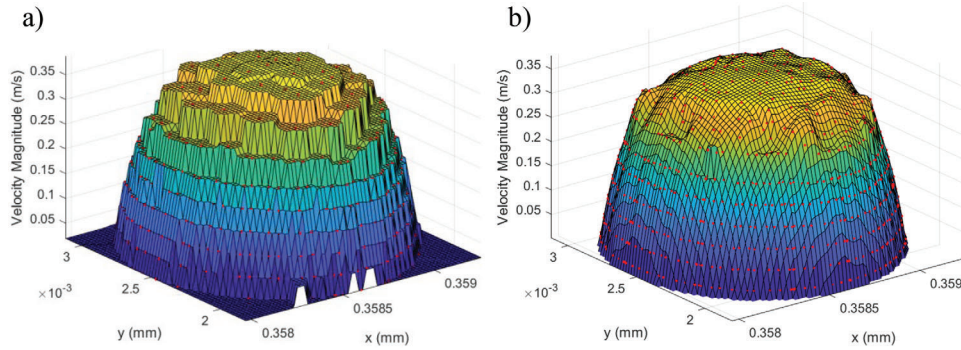
www.particle-journal.com

Figure 7. Surface graph of the interpolation results of a) nearest method; and b) RBF multi-quadric method.

Particle force balance equation:[58]

$$m_p \frac{\partial \boldsymbol{u}_p}{\partial t} = \boldsymbol{F}_{\text{drag}} + \boldsymbol{F}_{\text{gravitation}} + \boldsymbol{F}_{\text{Saffman lift}} \tag{9}$$

Drag force equation:[58]

$$\boldsymbol{F}_{\text{drag}} = m_p \frac{\boldsymbol{u} - \boldsymbol{u}_p}{\tau_r} \tag{10}$$

Gravitational force equation:[58]

$$\boldsymbol{F}_{\text{gravitation}} = m_p \, \boldsymbol{g} \frac{\rho_p - \rho}{\rho_p} \tag{11}$$

Saffman's lift force acting on particles equation:[59]

$$\boldsymbol{F}_{\text{Saffman lift}} = m_p \frac{2 K v^{1/2} \rho d_{ij}}{\rho_p d_p \left(d_{lk} d_{kl}\right)^{1/4}} \left(\boldsymbol{u} - \boldsymbol{u}_p\right) \tag{12}$$

2.3.2. Particle Modeling Parameter

For particle tracking and deposition analysis, three fractions are considered and calculated: the deposited particle diameter distribution (DD) fraction (Equation 13), which aims to show the penetration ability of particles with different diameters, the escaped particle diameter distribution (ED) fraction (Equation 14), which calculates the percentage of particles escaping from the outlets of the five lobes, and the escaped particle lobe distribution (EL) fraction (Equation 15) which calculates the percentage of particles escaping from the outlets of each lobe.

$$DD = \frac{\text{Mass of particle with diameter } d \text{ deposited in the region}}{\text{Total mass of particle with diameter } d \text{ injected}}$$
$$\times 100\% \tag{13}$$

$$ED = \frac{\text{Number of particle with diameter } d \text{ escaped from the outlets}}{\text{Total number of particle escaped from the outlets}}$$
$$\times 100\% \tag{14}$$

$$EL = \frac{\text{Number of particle escaped from the outlets of one lobe}}{\text{Total number of particle escaped from the outlets}}$$
$$\times 100\% \tag{15}$$

As the study by Kolanjiyil and Kleinstreuer[60] provided a particle-independence number of 3×10^6 aerosols per second, this study enforces the release of 3,000 particles in 0.01 s inside the left nasal cavity via a nozzle. In addition, the airflow velocity at the nostril inlet is set to 5 m s^{-1}, resulting in an instantaneous volume flow rate of 50 liters min^{-1}. A list of DPM modeling parameters is provided in **Table 7**.

2.3.3. Verification and Validation of Particle Deposition

The particle deposition fraction, representing the 1 to 10 μm aerosols cumulative deposition, is used to assess mesh convergence for the discrete phase in CFD simulations, as shown in **Figure 8**. Results indicate that the particle deposition fraction is similar for all 18 meshes, implying that mesh convergence has been achieved. Notably, the data from meshes T5, H5, and P5, which have two fewer boundary prism layers compared to the other meshes, exhibit no significant differences, suggesting that having four prism layers at density 4 is sufficient for solution convergence. Moreover, a closer look at the particle deposition fraction reveals that tetrahedral and hexahedral hybrid meshes yield comparable results. However, polyhedral hybrid meshes show ≈2% higher average nasal deposition and 2% lower average oral deposition. Nonetheless, for all other regions, the results of the polyhedral hybrid mesh align with those obtained from the tetrahedral and hexahedral meshes. In summary, grid convergence is evident, as fractions show minimal variation across all 18 meshes.

In addition, this study compared the particle deposition efficiency within the nasal cavity against previously reported experimental[66,67] and numerical[68–71] studies, as illustrated in Figure 8d. The normalized particle inertial parameter is a dimensionless parameter The inertial parameter is calculated as follows:

$$\text{Inertial Parameter} = d_p^2 \, Q \tag{16}$$

**ADVANCED
SCIENCE NEWS**

www.advancedsciencenews.com

Particle
& Particle Systems Characterization

www.particle-journal.com

Table 7. Particle tracking modeling parameters.

Parameters	Details	Refs.
Airflow inlet velocity	5 m s^{-1} (volume flow rate 50LPM)	–
Airflow outlet pressure	0 Pa	[46]
DPM tracking scheme	Implicit Euler (low order) and semi-implicit trapezoidal (high order)	[61]
Forces on particles	Drag (Equation 10), gravity (Equation 11), Saffman's lift (Equation 12)	[58,59]
Wall interaction	Trap	–
Turbulent dispersion	Discrete random walk	[62]
Particle release rate	3×10^6 aerosols per second	[60]
Particle density [kg m^{-3}]	998.2	–
Particle diameter [μm]	1–350	[44]
Particle diameter distribution	Rosin–Rammler (as shown in Figure S9, Supporting Information)	–
Drag Law	Spherical	[63]
Spray cone angle [deg]	30	[64]
Spray duration [s]	0.01	–
Nozzle diameter [mm]	0.5	[65]
Spray speed [m s^{-1}]	15	[65]
Total simulated time [s]	0.2	–

The findings from this investigation reveal that the particle deposition efficiency observed in the present work aligns well with the range reported in earlier experimental and numerical studies, demonstrating a similar trend. This consistency supports the reliability of the current model.

2.3.4. Verification and Validation of Airflow Dynamicsc

A comparison for validation is achieved with data obtained from previous experiments and CFD simulations. The output parameter is the total flow percentage, representing the percentage of airflow mass passing through each lobe or lung, as presented in **Table 8**. Results obtained from meshes T1 and H1 demonstrate a high degree of similarity, which can be attributed to the narrow regions, such as the bronchial tree, where generating a hexahedral mesh is challenging due to the limited space available. As a result, both meshes' structures in the model's lower portion are highly similar. Moreover, results from all three simulations (T1, H1, P1) are comparable, indicating that the meshes have likely reached convergence. However, while this is a positive indication, it is not conclusive proof of convergence. Finally, the data obtained from the present CFD simulation closely aligns with to or falls between the maximum and minimum values derived from earlier experimental and CFD data. This alignment serves to validate the reliability of the current CFD data. Therefore, the comparison with previous experimental and simulation data of the total flow percentage confirms the credibility of our CFD simulation.

3. Results and Discussion

3.1. 1D and 2D Grid Independence Test

Six planes representing distinct regions in the nasal-to-lung respiratory tract are positioned as shown in **Figure 9**. Planes A, B, C, D, E, and F are located in the nasal cavity, oral cavity, larynx, trachea, bronchi, and terminal bronchioles, respectively. Visual presentation of the velocity magnitude grid data for the selected planes derived from meshes with different densities and element types are presented in Figures S5 and S6 (Supporting Information).

Convergence of 1D data is indicated by minimal blank space between two or more adjacent lines. The center lines of planes C, D, and F are selected for comparison, as shown in **Figure 10**a–c, respectively.

The interpolated velocity magnitude results at the selected lines for various mesh types are displayed in **Figures 11** and S7 (Supporting Information). Since the velocity lines coincide in Figure 11a,b for tetrahedral and hexahedral meshes of varying densities, density-1 is sufficient for mesh convergence at planes C and D (larynx and trachea). However, slight discrepancies are observed between the polyhedral mesh densities in Figure 11c. The maximum difference between density 1 and 4 velocity magnitude is less than 0.025 m/s for tetrahedral and hexahedral hybrid meshes. However, for polyhedral meshes, the interpolated data for densities 1 and 2 differ significantly from those of densities 3 and 4, particularly at the line's midpoint. This discrepancy is attributed to the RBF interpolation scheme's overshoot or overprediction caused by the sparse cell distribution in the model's interior region due to the low-density polyhedral mesh and a volume density growth factor of 1.2. Consequently, density 3 may not achieve mesh convergence at plane F for the polyhedral hybrid mesh. Finally, Figure 11d compares the highest density data for each element type, demonstrating that all mesh element types can reach a consistent solution. Subsequently, residuals of the velocity magnitude at each plane are calculated for further analysis of polyhedral mesh convergence and quantification of the distance between 2D data sets.

For the 2D grid-independence test, residuals that determine solution convergence and provide insight into the magnitude and tendency of variations are calculated for the Nearest Neighbor
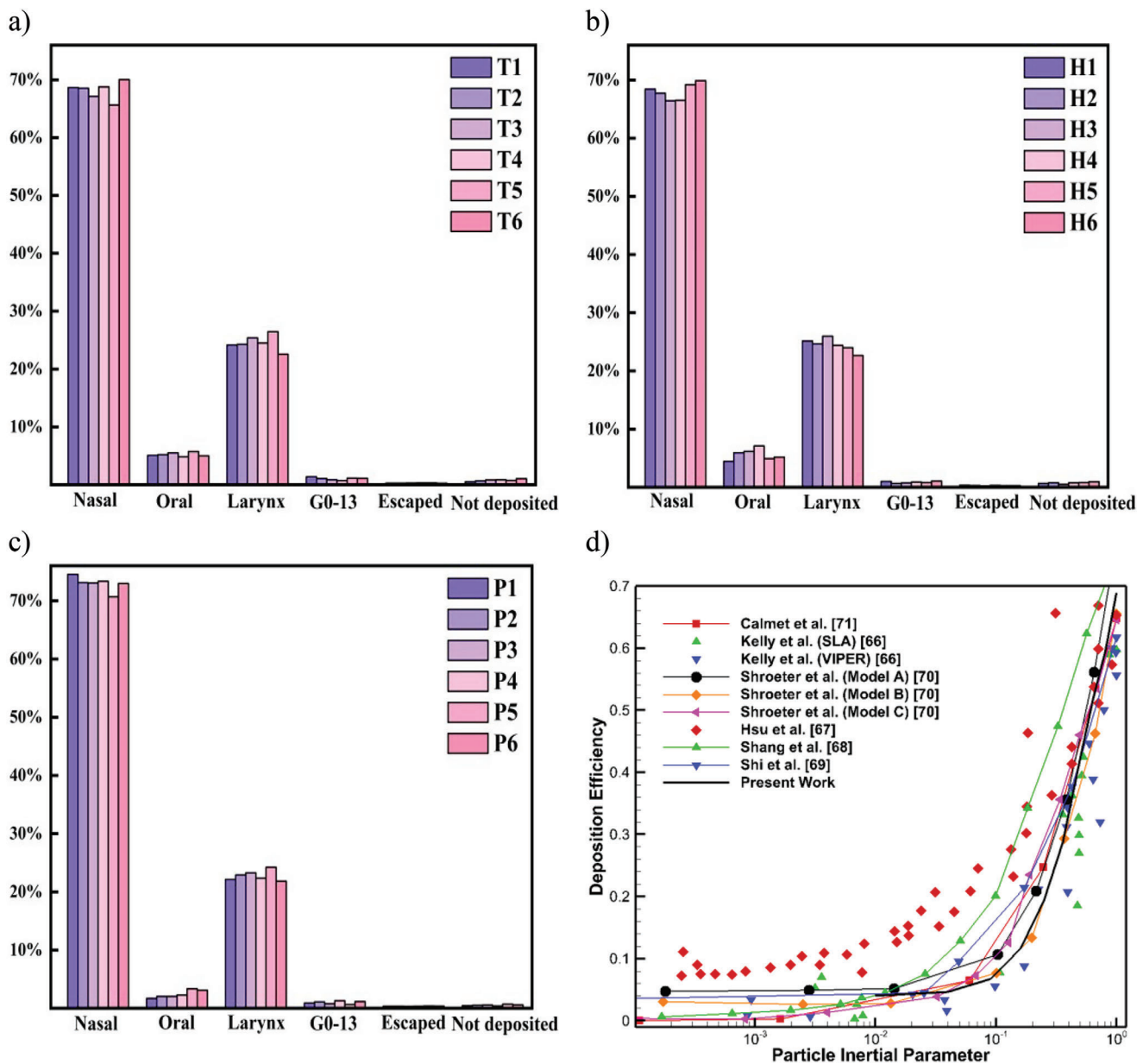
Figure 8. Particle deposition fraction of 1 to 10 µm aerosols (cumulative) in a) tetrahedral hybrid meshes, b) hexahedral hybrid meshes, and c) polyhedral hybrid meshes. The particle deposition efficiency in the nasal cavity is compared to the previous experimental and numerical data for validation in (d).

Table 8. A CFD and experimental comparison of the total flow rate percentage.

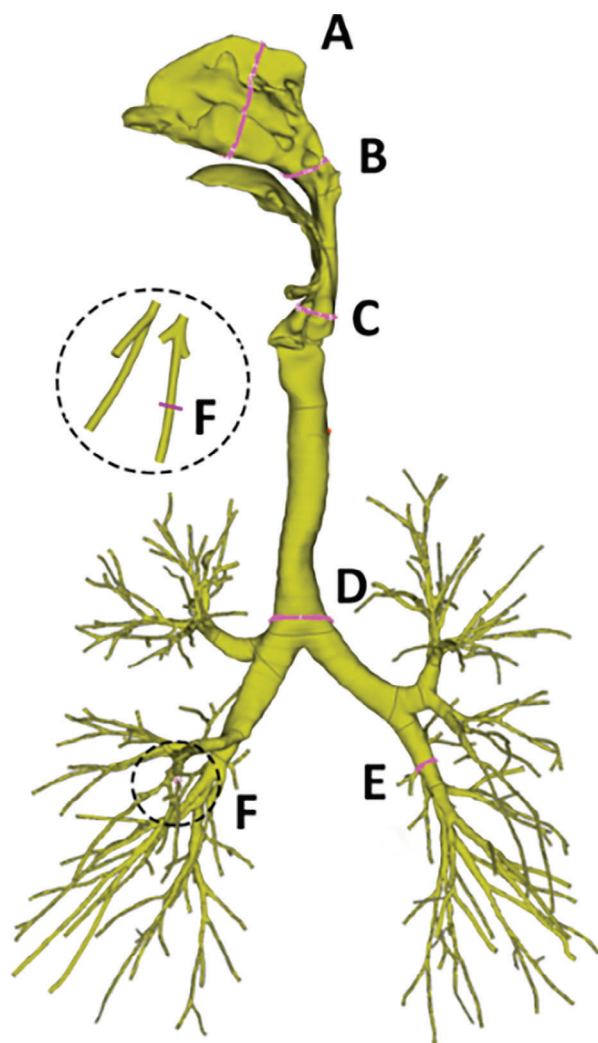| Total Flow (%)	Previous experiments		Previous CFD	Present CFD		
Regions	Cohen et al.[72]	Horsfield et al.[73]	Islam et al.[74]	T1	H1	P1
Left superior lobe	15.7	20.5	23.38	21.532	21.532	21.581
Left inferior lobe	24.3	24.9	21.82	20.928	20.925	20.967
Right superior lobe	18.5	21.7	21.03	23.120	23.124	23.044
Right middle lobe	9.2	9.6	9.953	11.092	11.091	11.099
Right inferior lobe	32.3	23.2	23.95	23.328	23.328	23.308
Left Lung	40	45.4	45.2	42.460	42.457	42.548
Right Lung	60	54.6	54.93	57.540	57.543	57.452

Figure 9. Six selected planes (A, B, C, D, E, and F) in different regions of the respiratory tract geometry.

addition, only the hexahedral mesh achieved an average residual below 5% for the Nearest Neighbor approach. Conversely, the RBF method maintained average residuals below 5% for all mesh element types and generally produced lower average residuals than the Nearest Neighbor. The discrepancy is partly attributed to the inherent errors of the latter interpolation scheme.

3.2. Optimal Numerical Solver and Mesh Combination

A comparison is conducted to evaluate the efficacy of pressure-velocity coupling schemes on the three mesh designs. **Table 11** compares the results of four different coupling schemes: Semi-Implicit Method for Pressure-Linked Equations (SIMPLE), Semi-Implicit Method for Pressure Linked Equations Consistent (SIMPLEC), Pressure-Implicit with Splitting of Operators (PISO), and Coupled Algorithm. The iterations and wall-clock time data in the table are the simulation iterations and time required for all CFD residuals to reduce below 0.001. Results show that the PISO scheme diverges for all meshes after approximately 100 iterations as the mesh quality for such a complex and large model is insufficient for the PISO algorithm. In addition, the iteration count and calculation time for tetrahedral simulations are 30% greater for SIMPLEC than for SIMPLE. The coupled scheme, however, requires less iteration but significantly more calculation time. Moreover, for hexahedral simulations, the SIMPLEC scheme calculates 19.8% faster than the SIMPLE scheme despite having the same number of iterations. The COUPLED scheme took longer to compute but is 39% faster than tetrahedral mesh. For all coupling schemes, the polyhedral hybrid mesh requires 2 to 4 times less time to compute than tetrahedral and hexahedral meshes. In conclusion, the combination of SIMPLE and polyhedral hybrid mesh achieves the best performance in terms of computation time reduction.

3.3. Airflow and Particle Dynamics

3.3.1. Particle Range: 1–10 μm

Figure 13 provides a detailed depiction of aerosols' locations after their conical-shaped release, offering valuable insights into their behavior within the respiratory tract. At the 0.01-second mark, aerosols are still being delivered into the nasal cavity (Figure 13a). At 0.02 s, particles either settle in the anterior region of the nasal cavity or move toward the posterior region. Notably, larger aerosols tend to congregate toward the rear of the nasopharynx and oropharynx, positioning themselves for potential collision with the cavity wall (Figure 13b,c). Meanwhile, smaller aerosols are conspicuously situated in the anterior portion of these regions. This intriguing separation between large and small aerosols can be elucidated through a particle force balance analysis.

The driving force foraerosols is the drag force exerted by the airflow, which is directly proportional to the first order of the aerosol's diameter. Conversely, the mass of aerosols scales with the third order of their diameter. Consequently, the acceleration of the aerosols is inversely proportional to the square of their diameter. Under similar conditions, such as maintaining the same
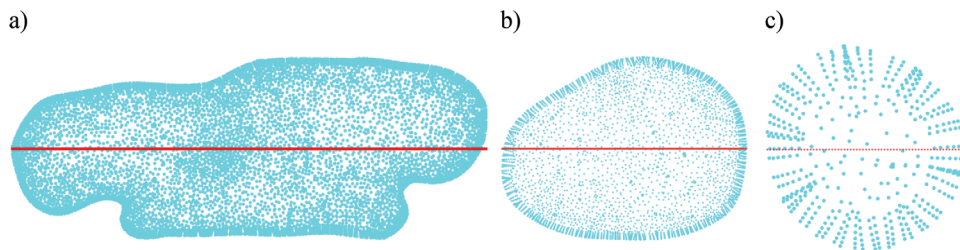
and RBF multi-quadric schemes, as shown in **Tables 9** and **10**, respectively. Mesh convergence is achieved for the five planes A to E since the residual values of the velocity magnitude are maintained below 5%. However, at plane F, residuals are greater than 5%, suggesting that the current mesh density is insufficient to achieve mesh convergence in the terminal bronchiole region. A comparison between the residuals from the two tables indicates that the Nearest Neighbor method yields higher residuals than the RBF method. This difference primarily stems from the interpolation technique, as the previously mentioned abnormal characteristics tend to lead to more significant discrepancies. Interpolation schemes with fewer unrealistic predictions yield highly accurate residuals. Based on this comparison, the Nearest Neighbor scheme used in the previously mentioned study[3] is prone to higher error. The visualization of RBF interpolation on 2D planes can be seen in Figure S8 (Supporting Information).

Figure 12 illustrates the variation in averaged residuals during coarse to fine mesh refinement. Except for tetrahedral hybrid meshes, all residuals decrease as the mesh density increases. In

ADVANCED
SCIENCE NEWS

www.advancedsciencenews.com

Particle
& Particle Systems Characterization

www.particle-journal.com

Figure 10. Three sets of 1D data (red lines) located at the center of a) plane C; b) plane D; and c) plane F.
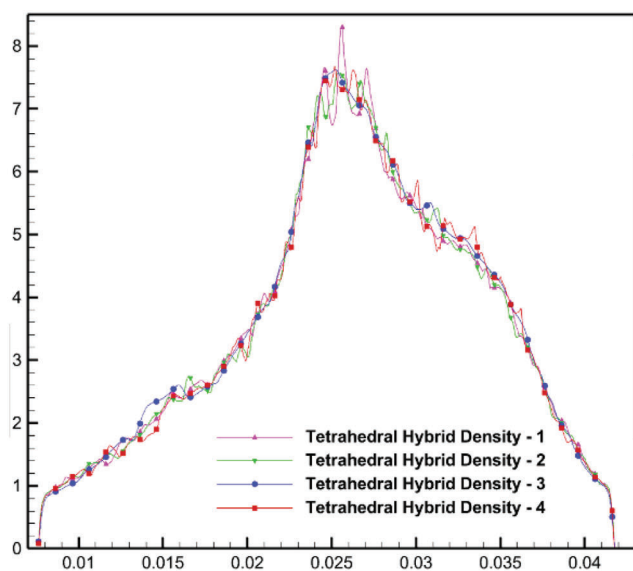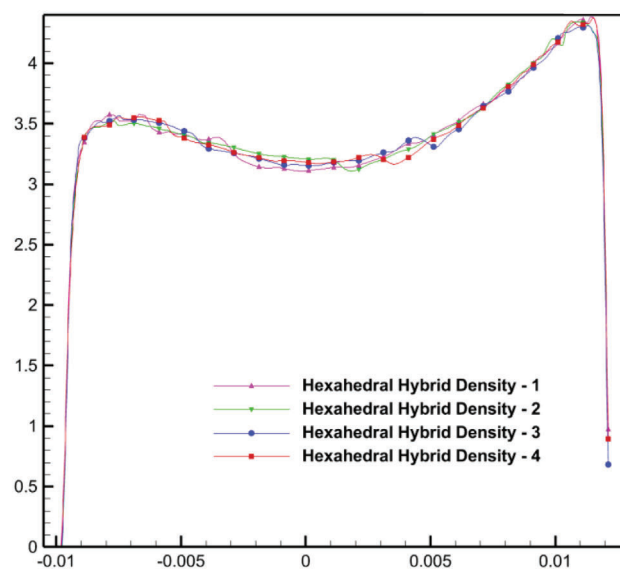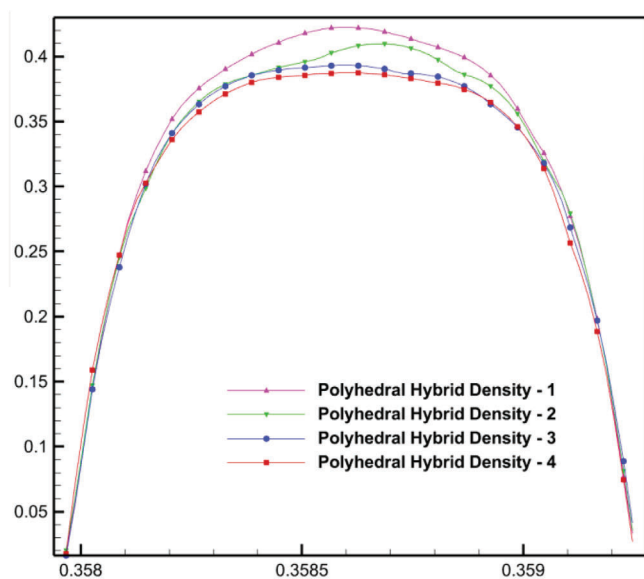
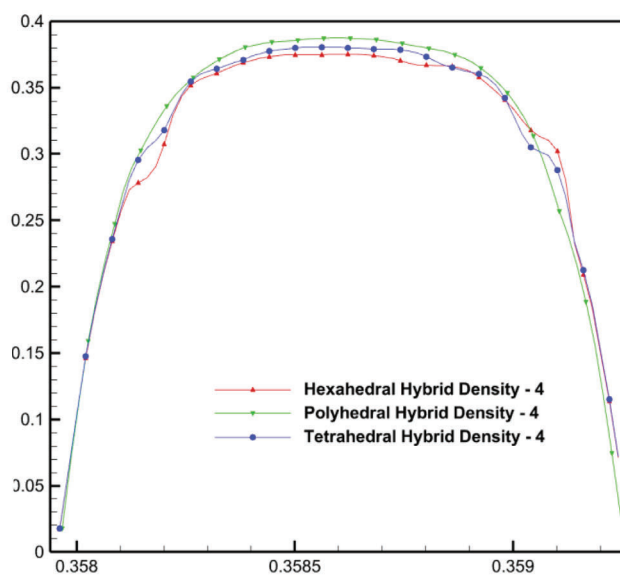**Figure 11.** 1D velocity magnitude comparison of different mesh types with varying densities. a) T1 to T4 data at the plane C line; b) H1 to H4 data at the plane D line; and c) P1 to P4 data at the plane F line. The above line charts compare simulation results from meshes with different densities, whereas d) H4, P4, and T4 at the plane F line.

Table 9. Residuals (%) calculated using Nearest Neighbor interpolation scheme.

Nearest Neighbor		Plane A	Plane B	Plane C	Plane D	Plane E	Plane F
Tetrahedral Hybrid	Density – 1 to 2	3.95	5.60	3.70	2.67	2.50	10.35
	Density – 2 to 3	4.55	7.37	4.49	2.74	3.08	11.34
	Density – 3 to 4	4.46	7.02	4.42	2.67	2.88	10.12
Hexahedral Hybrid	Density – 1 to 2	3.96	3.77	6.07	2.81	2.67	13.15
	Density – 2 to 3	3.53	3.74	5.99	2.44	2.80	12.77
	Density – 3 to 4	3.19	3.05	5.40	2.18	2.40	9.37
Polyhedral Hybrid	Density – 1 to 2	4.98	4.87	8.20	3.37	2.91	14.18
	Density – 2 to 3	4.79	4.71	8.05	3.05	3.22	14.86
	Density – 3 to 4	4.27	4.09	7.35	2.80	2.90	12.75

velocity difference between airflow and aerosol, smaller aerosols experience more significant velocity changes due to their larger acceleration. As a result, larger aerosols exhibit a slower velocity transition from horizontal to vertical direction at the nasopharynx and oropharynx regions, thereby segregating from their smaller counterparts.

Figure 13d reveals that the larynx area effectively filters out most of the remaining particles, allowing only a tiny fraction to enter the trachea and deeper airways. Subsequently, Figure 13e–g chronicle the progression of residual aerosols as they delve into the deeper lung generations. Only a few red spheres are visible, indicating that the larger aerosols have already been deposited. By the 0.08-second mark, the aerosols have traversed the entirety of the airway model, reaching the end and commencing their escape via the terminal bronchioles. As the aerosols progress through the respiratory tract, they consistently exhibit circular motion within the vicinity surrounding the vocal cords. This intriguing behavior suggests the presence of vortices or turbulent flow in these locations (**Figure 14**).

Two large vortices are formed at the partial laryngopharynx due to its upside-down pyramid shape interrupting the advancing airflow. The energetic presence of the vortices is sustained because of the narrow constricting gap at the larynx with wider areas above and below, creating a geometric configuration resembling that of a nozzle. As the airflow enters the constricted area, its velocity magnitude experiences a significant rise, reaching a remarkable value of 25 m s⁻¹. This results in the formation of a jet flow at the exit of the "nozzle", rushing downward into the expanded region of the upper trachea. The jet flow with

high velocity induces a downward movement of the surrounding air, while the air at lower positions reacts by flowing upward with a lower velocity, forming a 3D vortex due to the velocity gradient. Vortices, characterized by their notable rotating movement, are crucial in elevating aerosol deposition in the region. Smaller particles exhibit an extended duration of transport as the airflow advances them in a repetitive circular pattern. Conversely, larger particles with higher inertia undergo an alteration in their trajectory, resulting in collisions with the airway walls. As a result, no aerosol with a diameter greater than 7 µm deposited below the larynx, and a small aerosol deposition concentration site is observed both above and below the vocal cord (Figure 13h).

Figure 15 portrays cumulative aerosol deposition data in the nasal-to-lung respiratory tract using the P1 mesh configuration. In Figure 15a, a pronounced deposition pattern among large-diameter aerosols is discernible immediately following their release, predominantly depositing between the middle and inferior turbinate. This rapid deposition is attributed to the heightened kinetic energy (inertia) possessed by larger particles that exhibit greater resistance to the influence of airflow. Propelled by the pressure force of the spray at a velocity of 15 m s⁻¹, a few large-diameter particles exhibit a straight-line trajectory, exiting the nozzle and directly impacting the internal walls of the nasal cavity. Therefore, precise adjustments in position and spray angle of the nozzle can be made accordingly to target specific regions of interest. A wider spray angle, for instance, results in enhanced deposition at the anterior portion of the nasal cavity, while a narrower spray angle, combined with strategic

Table 10. Residuals (%) calculated using RBF-Multi Quadric interpolation scheme.

| RBF Multi-Quadric		Plane A	Plane B	Plane C	Plane D	Plane E	Plane F
Tetrahedral Hybrid	Density – 1 to 2	2.52	2.46	3.83	1.63	1.38	6.74
	Density – 2 to 3	3.01	2.53	4.16	1.73	1.48	6.16
	Density – 3 to 4	3.06	2.59	4.31	1.67	1.50	5.54
Hexahedral Hybrid	Density – 1 to 2	2.51	2.45	4.06	1.76	1.47	6.62
	Density – 2 to 3	2.30	2.45	4.18	1.68	1.36	6.01
	Density – 3 to 4	2.14	2.13	3.61	1.52	1.21	5.04
Polyhedral Hybrid	Density – 1 to 2	2.62	2.31	3.27	1.53	1.37	8.36
	Density – 2 to 3	2.44	2.26	3.21	1.42	1.22	7.48
	Density – 3 to 4	2.37	1.99	2.96	1.50	1.05	5.49
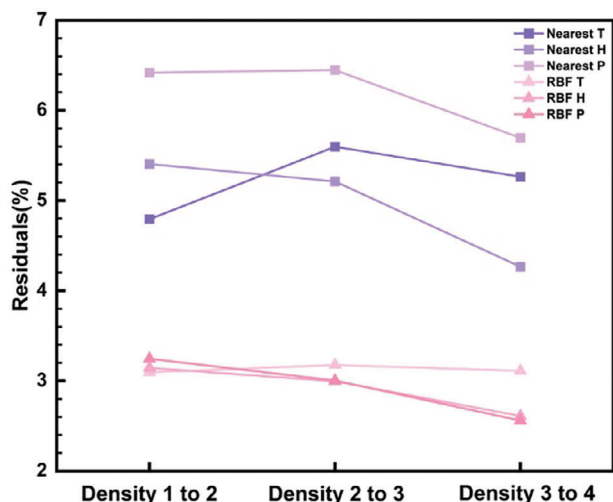
Figure 12. Variation of average residuals of the six selected planes from coarse to fine mesh.

positioning or inclination, can augment local aerosol deposition in the posterior nasal cavity region.

A second concentration site resulting from particle inertia emerges in the posterior portion of the superior turbinate. The geometry of the aforementioned region induces a sharp, ≈60-degree change in airflow direction. Aerosols traverse the nasal cavity horizontally, maintaining forward motion with slight deviations in direction owing to a combination of particle inertia and air drag forces. As the latter imparts a downward acceleration, the velocity vectors of large aerosols (8–10 μm) are not altered within a brief timespan, resulting in a concentrated deposition on the posterior surfaces of the nasopharynx and oropharynx. Conversely, the drag force-induced acceleration changes the direction of smaller aerosols (perfect advection), as acceleration magnitude is inversely proportional to the square of the diameter. Figure 15b depicts aerosol deposition concentration sites within the larynx region. Most large aerosols deposit above the vocal cords, while smaller aerosols (1–7 μm) traverse beyond the vocal cords and settle in regions below (Figure 15c,d). This phenomenon arises due to the narrowing geometry of the larynx, which increases the likelihood of large particle deposition above the vocal cords. Moreover, turbulence and vortices generated by the constricting geometry of the airflow facilitate aerosol deposition.

Figure 16 provides a comprehensive representation of the diameter distribution fractions of deposited aerosols obtained from the P1 simulation. An inversely proportional relationship exists between aerosol diameter and the percentage of escaped aerosols.

As aerosol diameter increases, the likelihood of particles escaping the distal lung generation outlets diminishes significantly, reaching a complete cessation for aerosols with diameters exceeding 7 μm. For larger aerosols, specifically those in the 8 to 10 μm range, the primary deposition site is the nasal cavity, accounting for a substantial deposition rate ranging from 52% to 69%. In contrast, medium-sized aerosols with diameters ranging from 4 to 7 μm predominantly deposit in the larynx, constituting 52% to 66% of their total deposition. However, smaller aerosols in the 1 to 3 μm range demonstrate a remarkable ability to pass through the larynx in substantial quantities, with deposition rates ranging from 57% to 76%. Additionally, the deposition pattern remains consistent across all five lobes of the respiratory system, with the majority of deposited aerosols falling within the 1 to 5 μm range.

Figure 17a illustrates the penetration ability of aerosols of varying diameters, where only aerosols possessing diameters <7 μm managed to traverse the entire length of the modeled airways successfully. Within the subset of escaped particles, those with diameters of 1 and 2 μm constituted 30.9% and 28.9% of the total, respectively. These findings strongly advocate for selecting aerosols with diameters around or below 1 μm to achieve deeper airway delivery. In Figure 17b, the percentage of aerosols that penetrated deeper generations within the five lobes reveals that smaller pharmaceutical aerosols exhibit a greater likelihood of reaching deeper generations within the right lobes, accounting for a substantial 66.2% of successful penetrations, compared to the left lobes, where the penetration rate is 33.8%. This observed difference is partially correlated with the distribution of airflow rates, where 57.5% is directed toward the right lobes and 42.5% toward the left lobes. Smaller aerosols follow fluid streamlines and consequently, the percentage of escaped particles correlates with that of the airflow.

3.3.2. Particle Range: 40–350 μm

All nasal sprayed pharmaceutical aerosols with a diameter >40 μm have deposited in the nasal cavity, as shown in **Figure 18**. This observation aligns with the expected deposition pattern observed for aerosols in the size range of 1–10 μm. Due to their increased kinetic energy, larger particles are more likely to rapidly deposit in the nasal cavity through inertial impaction. Remarkably, the simulation reveals that all aerosols in this size category deposit within a mere 0.02 s after their release. The swift deposition further supports the notion that aerosols with larger diameters exhibit enhanced deposition efficiency due to their higher momentum.

Table 11. A comparison of the performance of four different solver coupling schemes for each mesh type.

Pressure-velocity Coupling Scheme	Tetrahedral Hybrid		Hexahedral Hybrid		Polyhedral Hybrid	
	Iterations	Wall-clock time [s]	Iterations	Wall-clock time [s]	Iterations	Wall-clock time [s]
SIMPLE	152	1539.933	177	1988.803	100	650.902
SIMPLEC	197	1975.654	167	1594.579	103	662.745
PISO	DIVERGE		DIVERGE		DIVERGE	
Coupled	68	12105.924	53	7388.015	44	2982.765

**ADVANCED
SCIENCE NEWS**

www.advancedsciencenews.com

Particle
& Particle Systems Characterization
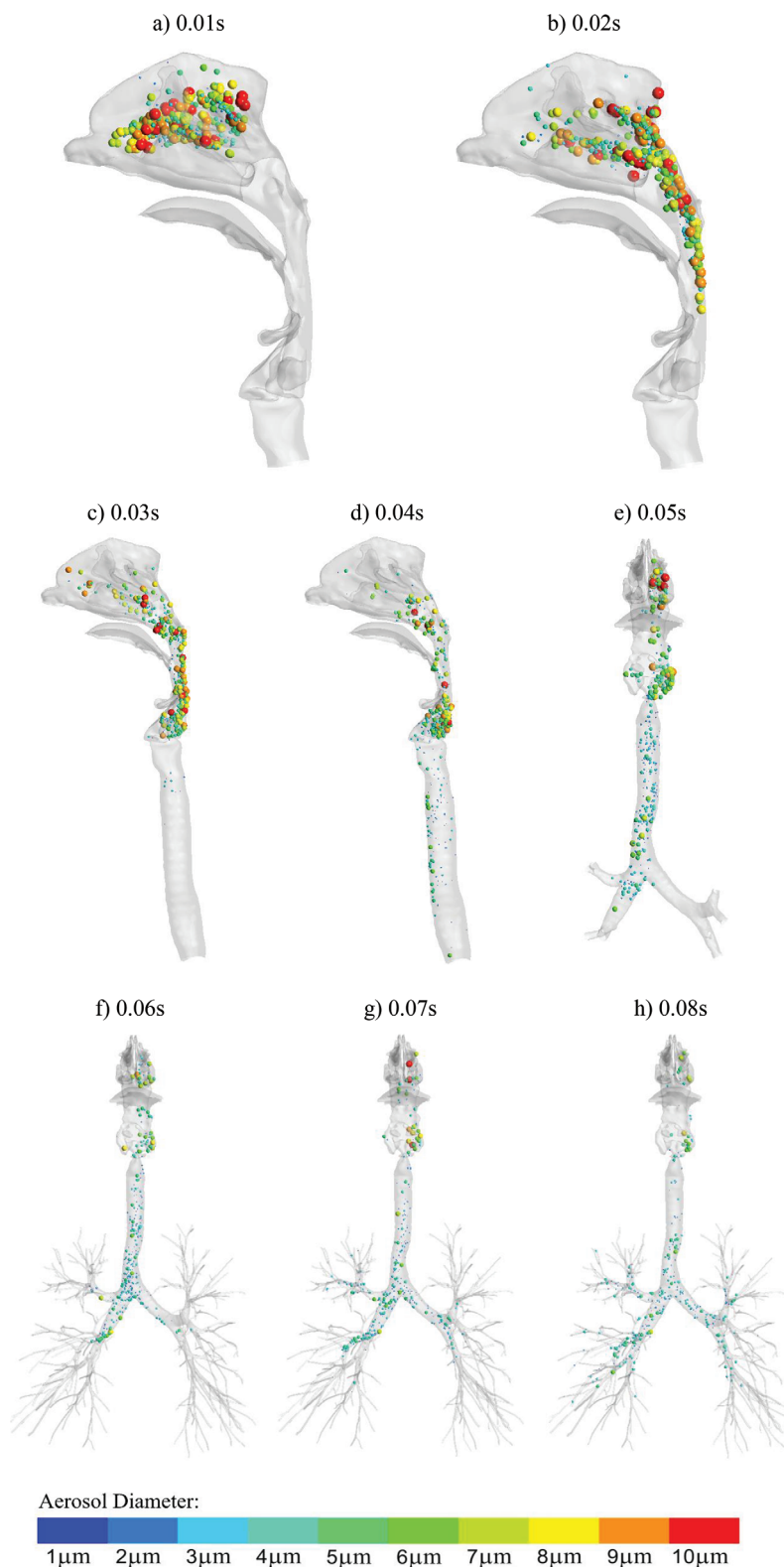
www.particle-journal.com

Figure 13. Aerosols' instantaneous positions in the respiratory tract using the P1 mesh configuration. Insets (a–h) show aerosols' locations at 0.01s to 0.08s of the breathing cycle, represented as spheres with color and size varying according to their diameter.
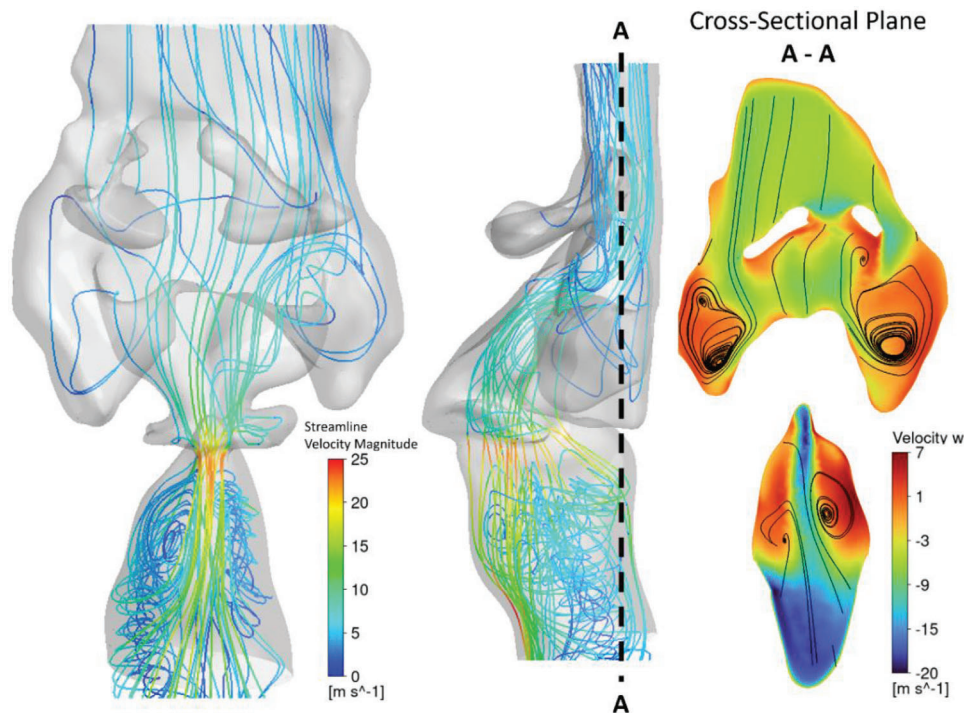
Figure 14. Airflow velocity magnitude and z-direction velocity and vortices at the larynx region.

Another significant remark is the lack of aerosol deposition observed in the nasopharynx area, namely the posterior part of the nasal cavity section. A noticeable deposition occurs in the nasopharynx for aerosols within the size range of 7–10 μm, but no deposition is observed for 40–350 μm particles in the exact location. This finding has significant implications for nasal medication administration, where targeted deposition within the nasal cavity is desirable for effective pharmaceutical outcomes. Therefore, for nasal spray targeting the posterior region of the nasal cavity or nasopharynx, such as intranasal steroids for allergic rhinitis treatment,[75] the spray should include aerosols with diameters ranging from 7–10 μm.

4. Conclusion

In this study, nasal sprayed aerosols were released in a realistic nasal-to-lung respiratory tract. The main findings are summarized as follows:

- Considering the output parameters of velocity magnitude and particle deposition, all examined meshes reach grid convergence. Calculation time is most affected by mesh element type, density, and boundary layer configuration. The best numerical approach for minimum calculation time is: Polyhedral hybrid unstructured mesh, four boundary prism layers with their first layer thickness control at 8% of the local surface nodal distance, density-1 configuration, and SIMPLE pressure-velocity coupling scheme.
- It is possible to compare unstructured data sets (including unstructured mesh topology and refinement) through inter-

polation. The use of various interpolation schemes, however, introduced different levels of error. The Nearest Neighbor interpolation scheme performed poorly on low-density data sets, whereas the RBF multi-quadric scheme provided a reasonable and seamless prediction for the gaps between the original data. The residual calculated during the comparison can serve as an indicator to examine the convergence condition of the targeted flow parameter in any dimension.
- Particle deposition is facilitated by the vortices and turbulent airflow above and below the larynx. A concentration site of deposited small (4–7 μm) aerosols is found at that location.
- Observing particle dynamics led us to the following conclusions regarding the optimal diameter for nasal-sprayed aerosols to target each region:
  1) Aerosols with diameters above 40 μm are deposited only in the nasal cavity.
  2) Aerosols with diameters ranging from 8 to 10 μm are deposited primarily (≈52% to 69%) in the nasal cavity and nasopharynx.
  3) Aerosols with diameters ranging from 4 to 7 μm are primarily deposited (roughly 52% to 66%) in the larynx region.
  4) Aerosols with diameters ranging from 1 to 3 μm passed the larynx (≈57% to 76%) and reached deeper lung generations.

5. Limitations

Some limitations of this study include: aerosols being modeled as ideal spheres, and simulations considering one-way fluid-particle
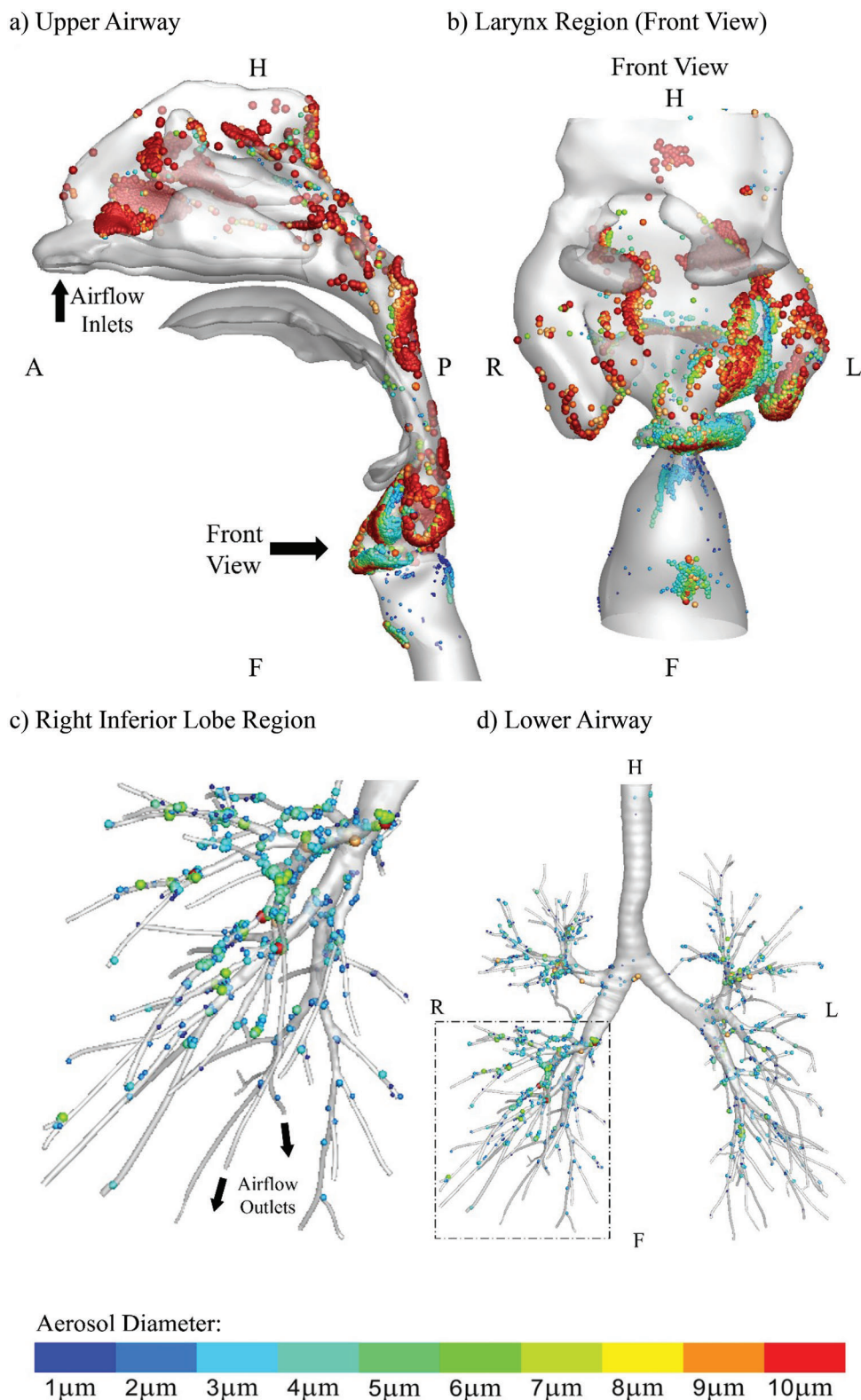
ADVANCED
SCIENCE NEWS

www.advancedsciencenews.com

Particle
& Particle Systems Characterization

www.particle-journal.com

Figure 15. Cumulative aerosol deposition in a) upper airway; b) larynx region; c) right inferior lobe region and d) lower airway. The orientations are labeled on the sides of the figures, where H, F, A, P, R, and L stand for head, feet, anterior, posterior, right, and left, respectively.
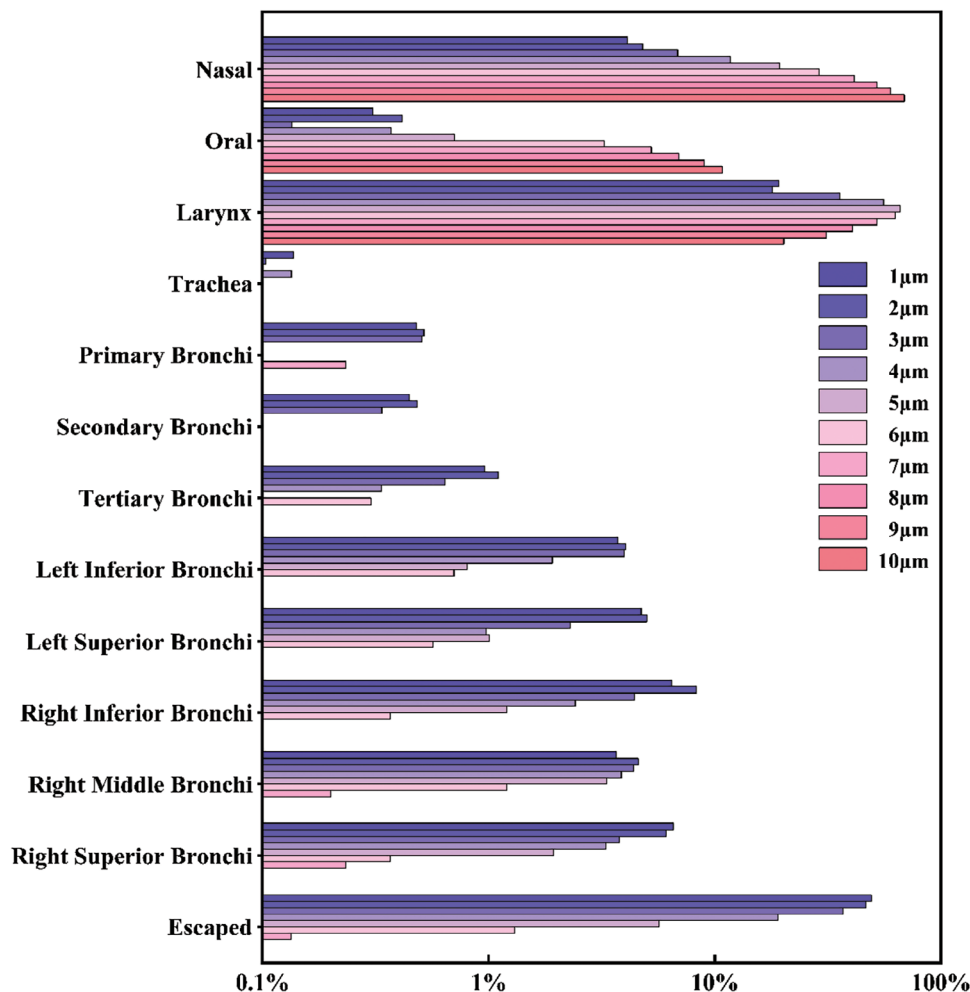
Figure 16. Deposited particle diameter distribution fraction.

coupling, meaning that only the fluid influences the particles whereas other interactions, such as particle collisions, are not modeled. In addition, the continuous fluid phase is idealized as a constant flow with a brief breathing duration of 0.2s, assuming that the inhalation flow rate does not undergo significant alterations during this period.

6. Future Studies

This study demonstrates that smaller nasal-released aerosols can reach deeper generations of the lung. Future research may examine aerosols with diameters <1 μm (nanoparticles). In addition, as varying levels of error induced by different interpolation
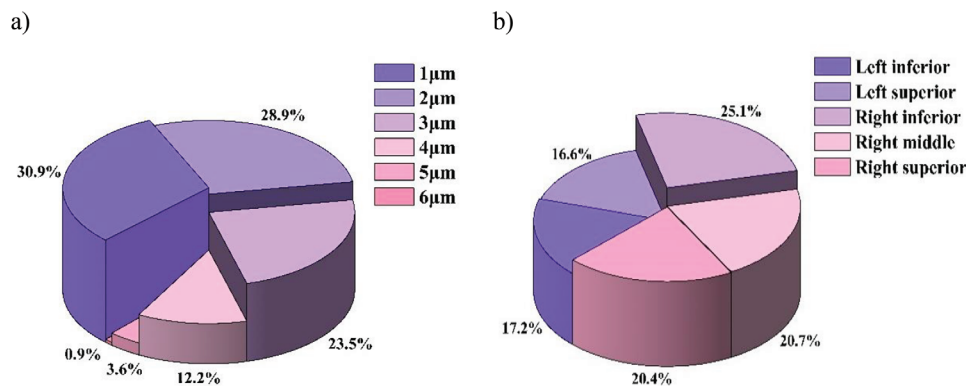

Figure 17. Escaped particle statistics: a) Escaped particle diameter distribution fraction and b) escaped particle lobe distribution fraction.

**ADVANCED
SCIENCE NEWS**

www.advancedsciencenews.com

Particle
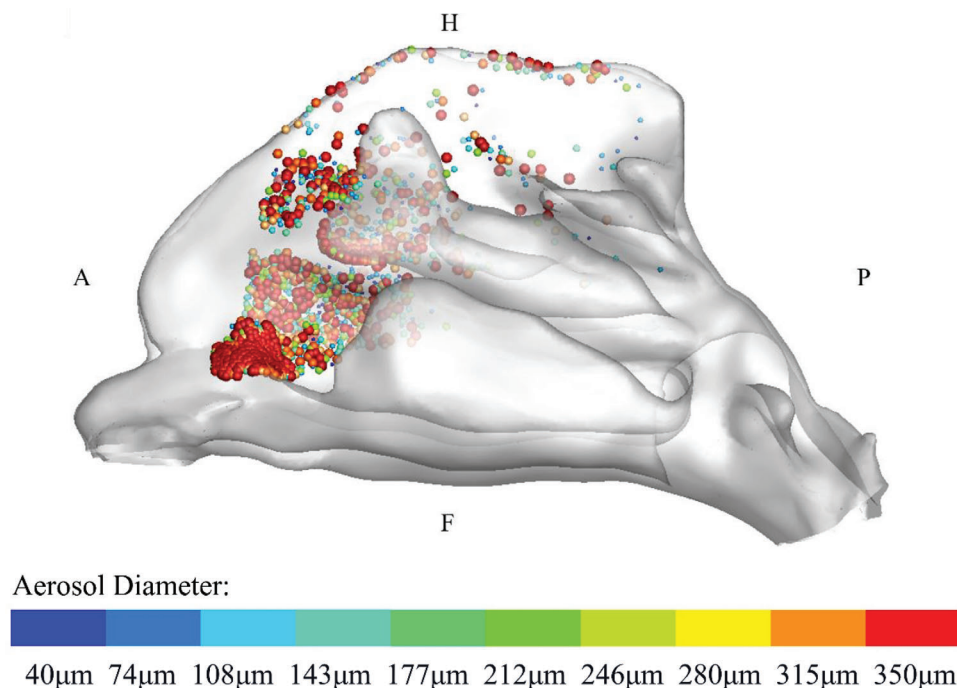& Particle Systems Characterization

www.particle-journal.com

Figure 18. Cumulative particle deposition in nasal cavity of aerosols with diameters ranging from 40 to 350 μm.

schemes have been observed, further research is required to determine the exact proportion of this error attributable to the interpolation scheme.

Appendix A: Mesh Quality

For the surface mesh, four quality criteria are used: FLUENT skewness of 0.5, I-DEAS warping of 40, FLUENT max angle quads of 0.5, and FLUENT max angle trias of 0.7. Both manual reconstructions of local mesh and automatic quality-fixing algorithms are applied to improve the surface mesh quality. Details of all surface mesh criteria mentioned above can be found in ref. [76]. The number of elements that did not meet the criteria is controlled below 3 for all cases. For volume mesh, five quality criteria are used: OpenFOAM skewness of 4, OpenFOAM warping of 0.8, ANSA Jacobian of 0.4, OpenFOAM non-orthogonality of 70, and OpenFOAM negative volume. Details of all volume mesh criteria mentioned above can be found in ref. [77]. An automatic quality-fixing algorithm is applied to improve volume mesh quality. The number of elements that did not meet the criteria is controlled below 1 in every 0.3 million cells.

Supporting Information

Supporting Information is available from the Wiley Online Library or from the author.

Conflict of Interest

The authors declare no conflict of interest.

Data Availability Statement

The data that support the findings of this study are available from the corresponding author upon reasonable request.

Keywords

aerosols, computational fluid-particle dynamics, multidimensional grid/mesh, nasal spray, respiratory tract

[1] X. Huang, L. M. Clemon, M. S. Islam, S. C. Saha, *Text. Res. J.* **2022**, *92*, 525.

[2] S. C. Saha, I. Francis, G. Saha, X. Huang, M. M. Molla, *Fluids* **2024**, *9*, 50.

[3] K. Inthavong, A. Chetty, Y. Shang, J. Tu, *Comput. Biol. Med.* **2018**, *102*, 40.

[4] M. M. Rahman, M. Zhao, M. S. Islam, K. Dong, S. C. Saha, *Adv. Powder Technol.* **2021**, *32*, 3506.

[5] Y. H. Kim, Z. B. Tong, H. K. Chan, R. Y. Yang, *J. Aerosol Sci.* **2019**, *134*, 14.

[6] M. M. Rahman, M. Zhao, M. S. Islam, K. Dong, S. C. Saha, *Eur. J. Pharm. Sci.* **2022**, *177*, 106279.

[7] M. Rahman, M. Zhao, M. S. Islam, K. Dong, S. C. Saha, *Powder Technol.* **2022**, *402*, 117364.

[8] R. Dutta, B. Spence, X. Wei, S. Dhapare, M. Hindle, P. W. Longest, *Pharm. Res.* **2020**, *37*, 199.

[9] P. Das, E. Nof, I. Amirav, S. C. Kassinos, J. Sznitman, *PLoS One* **2018**, *13*, 0207711.

[10] T. Gemci, V. Ponyavin, R. Collins, T. E. Corcoran, S. C. Saha, M. S. Islam, *Atmosphere* **2022**, *13*, 726.

[11] X. Huang, S. C. Saha, G. Saha, I. Francis, Z. Luo, *Environ. Adv.* **2024**, *16*, 100525.

[12] J. Wedel, P. Steinmann, M. Strakl, M. Hribersek, Y. Cui, J. Ravnik, *Comput. Methods Appl. Mech. Eng.* **2022**, *401*, 115372.

[13] M. B. Dolovich, A. Kuttler, T. J. Dimke, O. S. Usmani, *Int. J. Pharm. X* **2019**, *1*, 100018.

[14] K. Bass, S. Boc, M. Hindle, K. Dodson, W. Longest, *J Aerosol Med. Pulm. Drug Deliv.* **2019**, *32*, 132.

[15] K. Ahookhosh, M. Saidi, M. Mohammadpourfard, H. Aminfar, H. Hamishehkar, A. Farnoud, O. Schmid, *Eur. J. Pharm. Sci.* **2021**, *164*, 105911.

[16] P. G. Koullapis, M. Strakl, M. Hribersek, J. Ravnik, *J. Aerosol Sci.* **2020**, *144*, 105541.

[17] J. Wedel, P. Steinmann, M. Strakl, M. Hribersek, J. Ravnik, *Comput. Mech.* **2021**, *67*, 1497.

[18] D. O. Frank, J. S. Kimbell, S. Pawar, J. S. Rhee, *Otolaryngol. Head Neck Surg.* **2012**, *146*, 313.

[19] K. Inthavong, Q. Ge, C. M. K. Se, W. Yang, J. Y. Tu, *J. Aerosol Sci.* **2011**, *42*, 100.

[20] A. Rygg, M. Hindle, P. W. Longest, *J. Pharm. Sci.* **2016**, *105*, 1995.

[21] A. Rygg, M. Hindle, P. W. Longest, *Pharm. Res.* **2016**, *33*, 909.

[22] H. Calmet, D. Oks, A. Santiago, G. Houzeaux, A. L. Corfec, L. Deruyver, C. Rigaut, P. Lambert, B. Haut, J. Goole, *Int. J. Pharm.* **2022**, *626*, 122118.

[23] J. A. Keeler, A. Patki, C. R. Woodard, D. O. Frank-Ito, *J. Aerosol Med. Pulm. Drug Deliv.* **2016**, *29*, 153.

[24] K. Ahookhosh, S. Yaqoubi, M. Mohammadpourfard, H. Hamishehkar, H. Aminfar, *Int. J. Pharm.* **2019**, *566*, 157.

[25] B. K. Huynh, D. Traini, D. R. Farkas, P. W. Longest, M. Hindle, P. M. Young, *J. Aerosol Med. Pulm. Drug Deliv.* **2018**, *31*, 103.

[26] N. Khajeh-Hosseini-Dalasm, P. W. Longest, *J. Aerosol Sci.* **2015**, *79*, 15.

[27] P. W. Longest, K. Bass, R. Dutta, V. Rani, M. L. Thomas, A. El-Achwah, M. Hindle, *Expert Opin. Drug Deliv.* **2019**, *16*, 7.

[28] P. W. Longest, G. Tian, N. Khajeh-Hosseini-Dalasm, M. Hindle, *J. Aerosol Med. Pulm. Drug Deliv.* **2016**, *29*, 461.

[29] J. Wedel, P. Steinmann, M. Strakl, M. Hribersek, J. Ravnik, *Comput. Mech.* **2021**, *67*, 1497.

[30] K. Bass, P. W. Longest, *J. Aerosol Sci.* **2018**, *119*, 31.

[31] J. Xi, P. W. Longest, *Ann. Biomed. Eng.* **2007**, *35*, 560.

[32] P. W. Longest, J. Xi, *Aerosol Sci. Technol.* **2007**, *41*, 380.

[33] X. A. Si, M. Sami, J. Xi, *Pharmaceutics* **2021**, *13*, 903.

[34] X. A. Si, J. Xi, in *Modeling of Mass Transport Processes in Biological Media* (Ed: S. Becker, A. V. Kuznetsov, F. Monte, G. Pontrelli, D. Zhao), **2022**, Academic Press, San Diego, California, pp. 311–333.

[35] J. Xi, P. W. Longest, *Int. J. Heat Mass Transfer* **2008**, *51*, 5562.

[36] B. Soni, D. Thompson, *36th AIAA Fluid Dynamics Conf. and Exhibit*, San Francisco, California, June **2006**.

[37] P. W. Longest, S. Vinchurkar, *Med. Eng. Phys.* **2007**, *29*, 350.

[38] S. Vinchurkar, P. W. Longest, *Comput. Fluids* **2008**, *37*, 317.

[39] B. Soni, N. Arra, S. Aliabadi, W. Luke, K. Walters, presented at 20th AIAA Computational Fluid Dynamics Conf., Honolulu, **2011**.

[40] M. Zubair, M. Z. Abdullah, K. A. Ahmad, *Computational and Mathematical Methods in Medicine* **2013**, *2013*, 727362.

[41] D. O. Frank-Ito, M. Wofford, J. D. Schroeter, J. S. Kimbell, *J Aerosol Med Pulm Drug Deliv* **2016**, *29*, 46.

[42] B. Kumar, V. Srivastav, A. Jain, A. Paul, Int. J. Integr. Eng. **2019**: p. 32.

[43] G. Tian, M. Hindle, S. Lee, P. W. Longest, *Pharm. Res.* **2015**, *32*, 3170.

[44] K. Inthavong, W. Yang, M. Fung, X. Tong, J. Tu, presented at 19th Australasian Fluid Mechanics Conf., Melbourne, Australia, December **2014**.

[45] E. R. Weibel, in *Morphometry of the Human Lung*, Springer, Berlin, Heidelberg, **1963**, pp. 110–135.

[46] S. C. Saha, I. Francis, X. Huang, A. R. Paul, *Phys. Fluids* **2022**, *34*.

[47] X. Huang, I. Francis, G. Saha, M.d. M. Rahman, S. C. Saha, *Results Eng.* **2024**, *23*, 102475.

[48] S. C. Saha, X. Huang, I. Francis, G. Saha, *Respiratory Physiol. Neurobiol.* **2024**, *325*, 104265.

[49] S. C. Saha, I. Francis, X. Huang, M. M. Rahman, *presented at Proceedings of the 23rd Australasian Fluid Mechanics Conf. (AFMC2023)*, Australasian Fluid Mechanics Society, Perth, Western Australia, December **2022**.

[50] P. J. Roache, *J. Fluids Eng.* **1994**, *116*, 405.

[51] The SciPy community, scipy.interpolate.NearestNDInterpolator, https://docs.scipy.org/doc/scipy/reference/generated/scipy. interpolate.NearestNDInterpolator.html#scipy.interpolate. NearestNDInterpolator, February, **2023**.

[52] A. Chirokov, *Scattered Data Interpolation and Approximation using Radial Base Functions*, https://www.mathworks.com/ matlabcentral/fileexchange/10056-scattered-data-interpolation- and-approximation-using-radial-base-functions, November, **2023**.

[53] C. D. Argyropoulos, N. C. Markatos, *Appl. Mathematical Model.* **2015**, *39*, 693.

[54] ANSYS, in *ANSYS Fluent Theory Guide*, ANSYS, Inc., Canonsburg, PA **2020**, pp. 2–3.

[55] ANSYS, in *ANSYS Fluent Theory Guide*, ANSYS, Inc., Canonsburg, PA, **2020**, pp. 3–4.

[56] ANSYS, in *ANSYS Fluent Theory Guide*, ANSYS, Inc., Canonsburg, PA, 2020, p. 59.

[57] ANSYS, in *ANSYS Fluent Theory Guide*, ANSYS, Inc., Canonsburg, PA, **2020**, p. 430.

[58] ANSYS, in *ANSYS Fluent Theory Guide*, ANSYS, Inc., Canonsburg, PA, **2020**, pp. 420–421.

[59] ANSYS, Saffman's Lift Force, in *ANSYS Fluent Theory Guide*, ANSYS, Inc., Canonsburg, PA, **2020**, p. 423.

[60] A. Kolanjiyil, C. Kleinstreuer, *J. Aerosol Sci.* **2017**, *114*.

[61] ANSYS, in *ANSYS Fluent User's Guide*, ANSYS, Inc., Canonsburg, PA, **2020**, p. 2009.

[62] ANSYS, in *ANSYS Fluent Theory Guide*, ANSYS, Inc., Canonsburg, PA, **2020**, p. 433.

[63] ANSYS, in *ANSYS Fluent Theory Guide*, ANSYS, Inc., Canonsburg, PA, **2020**, p. 432.

[64] J. Van Strien, P. Petersen, P. Lappas, L. Yeo, S. Rezk, S. Vahaji, K. Inthavong, *J. Aerosol Sci.* **2022**, *165*, 106009.

[65] K. Inthavong, Z. F. Tian, J. Y. Tu, W. Yang, C. Xue, *Comput. Biol. Med.* **2008**, *38*, 713.

[66] J. T. Kelly, B. Asgharian, J. S. Kimbell, B. A. Wong, *Aerosol Sci. Technol.* **2004**, *38*, 1063.

[67] D.-J. Hsu, M.-H. Chuang, *Aerosol Sci. Technol.* **2012**, *46*, 631.

[68] Y. Shang, K. Inthavong, J. Tu, *Comput. Fluids.* **2015**, *114*, 141.

[69] H. Shi, C. Kleinstreuer, Z. Zhang, *J. Aerosol Sci.* **2007**, *38*, 398.

[70] J. D. Schroeter, G. J. Garcia, J. S. Kimbell, *J. Aerosol Sci.* **2011**, *42*, 52.

[71] H. Calmet, K. Inthavong, B. Eguzkitza, O. Lehmkuhl, G. Houzeaux, M. Vázquez, *PLoS One* **2019**, *14*, 0221330.

[72] B. Cohen, R. Sussman, M. Lippmann, *Aerosol Sci. Technol.* **1990**, *12*, 1082.

[73] K. Horsfield, G. Dart, D. E. Olson, G. F. Filley, G. Cumming, *J. Appl. Physiol.* **1971**, *31*, 207.

[74] M. S. Islam, S. C. Saha, E. Sauret, T. Gemci, Y. T. Gu, *J. Aerosol Sci.* **2017**, *108*, 29.

ADVANCED
SCIENCE NEWS

www.advancedsciencenews.com

Particle
& Particle Systems Characterization

www.particle-journal.com

[75] M. D. Seidman, R. K. Gurgel, S. Y. Lin, S. R. Schwartz, F. M. Baroody, J. R. Bonner, D. E. Dawson, M. S. Dykewicz, J. M. Hackell, J. K. Han, S. L. Ishman, H. J. Krouse, S. Malekzadeh, J. W. Mims, F. S. Omole, W. D. Reddy, D. V. Wallace, S. A. Walsh, B. E. Warren, M. N. Wilson, L. C. Nnacheta, *Otolaryngol. Head Neck Surg.* **2015**, *152*, S1.

[76] BETA CAE Systems, in *ANSA version 22.0.x User Guide. 2020: BETA CAE Systems International AG, D4 Business Village*, Switzerland, pp. 879–890.

[77] BETA CAE Systems, in *ANSA version 22.0.x User Guide. 2020: BETA CAE Systems International AG, D4 Business Village*, Switzerland, pp. 1073–1080.